

Supplementary Materials: Light-induced ideal Weyl semi-metal HgTe via nonlinear phononics

Dongbin Shin,^{1,2,*} Angel Rubio,^{2,3,4,†} and Peizhe Tang^{5,2,‡}

¹*Department of Physics and Photon Science,
Gwangju Institute of Science and Technology (GIST), Gwangju 61005, Republic of Korea*

²*Max Planck Institute for the Structure and Dynamics of Matter and
Center for Free Electron Laser Science, 22761 Hamburg, Germany*

³*Nano-Bio Spectroscopy Group, Departamento de Física de Materiales,
Universidad del País Vasco UPV/EHU- 20018 San Sebastián, Spain*

⁴*Center for Computational Quantum Physics (CCQ),
The Flatiron Institute, 162 Fifth avenue, New York NY 10010*

⁵*School of Materials Science and Engineering,
Beihang University, Beijing, China*

CONTENTS

| | |
|--|----|
| List of Tables | 2 |
| List of Figures | 2 |
| Computational details | 5 |
| Lattice parameter and Phonon eigen vectors of IR modes | 6 |
| Electronic structure of optimized geometry in bulk HgTe, HgSe, and HgS | 7 |
| Plasmon frequency in bulk HgTe | 7 |
| Meta-stable geometry induced by THz pulse and role of dissipation | 8 |
| Nonlinear Phonon interaction in the simplified model | 8 |
| Weyl points in the Fermi arc surface states | 10 |
| Symmetry analysis and Berry curvature dipole | 10 |
| Screening effect by static electric field on HgTe | 13 |
| Nonlinear phonon interaction; detail and examples | 15 |
| Effect of static electric field on HgTe | 15 |
| Phonon dispersion in bulk HgTe family | 17 |
| References | 17 |

LIST OF TABLES

| | | |
|----|--|----|
| S1 | Computed parameters of HgTe, HgSe, and HgS structure from DFT calculations. | 20 |
| S2 | Parameters for the model simulation in HgTe, HgSe, and β -HgS. | 21 |

LIST OF FIGURES

| | | |
|----|--|----|
| S1 | Conversion of Cartesian vectors in primitive lattice to cubic lattice. a , Cartesian vectors (red) and lattice vectors (blue) in primitive lattice. b , Cartesian vectors of the primitive lattice (red) in cubic lattice and lattice vectors of cubic lattice. | 22 |
|----|--|----|

| | | |
|-----|--|----|
| S2 | Band structure of HgS, HgSe, and HgTe. a-c , Band structure calculated with PBE functional of (a) HgS, (b) HgSe, and (c) HgTe. | 23 |
| S3 | THz-field induced distorted geometry through the nonlinear phonon interaction through the <i>ab initio</i> MD simulation in normal coordinate. a, Time profile of THz-field induced dynamics in bulk HgTe. b, Time profile of THz-field induced dynamics in bulk HgSe. c, Time profile of THz-field induced dynamics in bulk β -HgS. | 24 |
| S4 | THz-field induced distorted geometry through the nonlinear phonon interaction through the <i>ab initio</i> MD simulation in Cartesian coordinate. a-b, Time profile of THz-field induced dynamics for (a) Hg and (b) Te in bulk HgTe. c-d, Time profile of THz-field induced dynamics for (c) Hg and (d) Se in bulk HgSe. e-f, Time profile of THz-field induced dynamics for (e) Hg and (f) S in bulk β -HgS. | 25 |
| S5 | Nonlinear phonon interaction between IR modes in HgTe. a, Time profile of nonlinear phonon dynamics evaluated with Model Hamiltonian simulation. b, Maximum amplitude of induced IR mode under the given initial IR_x mode. | 26 |
| S6 | THz-induced dynamics in simplified model without fractional dissipation. a-c, Time profile of THz-field induced dynamics in bulk (a) HgTe, (b) HgSe, and (c) β -HgS. | 27 |
| S7 | THz-induced dynamics in a simplified model with fractional dissipation. a-c, Time profile of THz-field induced dynamics in bulk (a) HgTe, (b) HgSe, and (c) β -HgS with various dissipation ratios. | 28 |
| S8 | THz-induced dynamics with constrained condition. a-b, Time-profile of averaged Hg and Te displacement (a) with, and (b) without thermostat. . | 29 |
| S9 | Fermi arc surface states of HgTe in the shifted equilibrium position by the nonlinear phononic interaction. a-c, Fermi arc surface states in (a) (100), (b) (010), and (c) (001) surface with $Q_{ind} = 0.5 \text{ \AA}\sqrt{\mu}$ in HgTe. .. | 30 |
| S10 | Fermi arc surface states of HgSe in the shifted equilibrium position by the nonlinear phononic interaction. a-c, Fermi arc surface states in (a) (100), (b) (010), and (c) (001) surface with $Q_{ind} = 0.5 \text{ \AA}\sqrt{\mu}$ in HgSe. .. | 31 |

| | | |
|-----|---|----|
| S11 | Fermi arc surface states of HgS in the shifted equilibrium position by the nonlinear phononic interaction. a-c, Fermi arc surface states in (a) (100), (b) (010), and (c) (001) surface with $Q_{ind} = 0.5 \text{ \AA}\sqrt{\mu}$ in HgS. . . . | 32 |
| S12 | Berry curvature near Weyl points in the atomic distorted HgTe. a-c, Berry curvature (a) Ω_x , (b) Ω_y , and (c) Ω_z at $k_z = 35.3 \text{ m\AA}^{-1}$ plane. . . | 33 |
| S13 | Field-induced forces in the HgTe slab. Schematics of electric field-induced forces via (a) Lorentz-type force and (b) length gauge field. The red arrows in (a) demonstrate the force directions on each atom obtained from Lorentz-type force. The saw-tooth-type potential is marked by red lines in (b). (c) Atomic geometry of the HgTe slab model. (d) The calculated density of state for (upper) the HgTe slab model and (bottom) the bulk HgTe. (e) Average and deviation values for calculated forces on each atom in HgTe thin film with the change of applied static electric field by using different methods. The deviation value is calculated for all Hg and Te atoms in the slab model. | 34 |
| S14 | The influence of screening effect on field-induced forces for the HgTe slab with charge doping. The calculated density of state for (a) the HgTe slab model with hole doping, (b) the pristine HgTe slab model, and (c) the HgTe slab model with electron doping. (d) Schematics of the saw-tooth-type potential applied to the HgTe slab model. The average values for calculated forces on each atom in the HgTe thin film with (e) hole doping and (f) electron doping under the saw-tooth-type electric potential, the force on each atom is calculated by using the length gauge field method. The dashed red lines indicate the Fermi level in (a)-(c). e is the absolute value of electron charge. | 35 |
| S15 | Phonon dispersion of (a) HgTe, (b) HgSe, and (c) β -HgS along with symmetry points | 36 |

Computational details

We used the Vienna Ab initio Simulation Package (VASP) to evaluate the lattice parameters, the electronic structure, and nonlinear phononics [1]. The plane-wave basis up to 400 eV was employed to describe the Kohn-Sham wavefunctions with spin-orbit coupling. The core level states were considered by the projector augmented wave method. We sampled the Brillouin zone with $10 \times 10 \times 10$ and $6 \times 6 \times 6$ grid points for primitive lattice and cubic cell geometries of HgTe, respectively. For the electron-electron exchange and correlation, we used Perdew-Zunger-type (PZ) local density approximation (LDA) functional [2]. The eigenvectors of the IR phonon modes were achieved in primitive lattice and converted into cubic geometry. To evaluate the topological properties of HgTe with the Wannier interpolation technique, we used Wannier90 and WannierTools packages [3, 4]. The Bloch states with 200×200 sampled grid points in the Brillouin zone were considered for the Fermi arc surface plot. The Berry curvature dipole was evaluated using in-house code with $80 \times 80 \times 80$ Bloch vector sampling [5].

To investigate the effect of the time-dependent THz field on the HgTe, we modified the AIMD simulation code to include the direct force from the applied laser pulse to the charged ion in the Quantum Espresso package [6]. We verified that the electronic structure and nonlinear phononics in the HgTe family are consistently evaluated in both VASP and Quantum Espresso. The effect of the time-dependent electric field on the ion under the periodic boundary condition was described by Lorentz force between the Born effective charge (Z_τ) for each atom and electric field ($\mathbf{E}(\mathbf{t})$) at a given time t as follows; $\mathbf{F}_\tau(\mathbf{t}) = Z_\tau \mathbf{E}(\mathbf{t})$. With this implementation, the Verlet algorithm in the $3 \times 3 \times 3$ supercell geometry of HgTe was used to include enough dissipation channels via phonon-phonon scatterings without a thermostat for the AIMD simulation. We considered a single gamma k-point sampling and the spin-unpolarized state. The projector augmented wave method and plane-wave basis up to 680 eV were employed to describe the Kohn-Sham states. We calculated the Born effective charges that are Hg ($3.18 e$) and Te ($-3.18 e$) atoms through the density functional perturbation theory calculation [7]. In the previous studies, the classical model Hamiltonian was employed to investigate the nonlinear phonon interactions that heavily relied on the limited fitting parameters for few phonon modes and frictional dissipation [8]. However, our new approach allows a simulation with realistic dynamics by including anharmonicity and

various phonon-phonon scatterings at the accuracy level of *ab initio* calculations. Overall, conventional AIMD simulations were carried out up to the 6 fs time step to investigate the nonlinear phonon interaction between IR modes. To evaluate the collective motions for the IR mode during conventional AIMD simulation, we evaluated the average displacements of Hg and Te atoms as follows: $\mathbf{Q}_{\text{IR}} = \sum_i^{N_{\text{cell}}} d(\mathbf{Q}_{\text{Hg}}^i - \mathbf{Q}_{\text{Te}}^i)/N_{\text{cell}}$, when $N_{\text{cell}} = 27$ and $d = 0.714$ are the number of repeated cell and a factor for the conversion between normal and Cartesian coordinates, respectively. In addition, we neglect the plasmon-phonon interaction and non-adiabatic dynamic effect for electronic structures under the Born-Oppenheimer approximation, because the frequency of the THz pulse (2.6 THz \sim 0.01eV) is far from the 3D plasmon frequency (0.53 THz) in *n*-type doped HgTe at low temperature [9].

Lattice parameter and Phonon eigen vectors of IR modes

We optimized the lattice parameters of HgTe, HgSe, and HgS and their inner atomic positions using DFT stress and force calculations. The calculated lattice parameters for primitive unit cell are $a = 4.559$ Å for HgTe, $a = 4.301$ Å for HgSe and $a = 4.122$ Å for HgS with LDA functional. The eigenvectors of IR phonon modes (e) and their frequencies (ω) are evaluated with these lattice parameters through the diagonalization of the dynamical matrix (D) with density functional perturbation theory as follows:

$$\sum_{j'\beta} D_{\alpha,\beta,\mathbf{q}} e_{\beta}(j', \mathbf{q}, \nu) = m_j [\omega(\mathbf{q}, \nu)]^2 e_{\alpha}(j, \mathbf{q}, \nu), \quad (1)$$

when j , $\alpha(\beta)$, \mathbf{q} , and ν are the indexes for atoms, the direction in the Cartesian coordinate, momentum, and phonon mode, respectively. The eigenvector of IR phonon mode at $\mathbf{q} = \Gamma$ is $e_{\alpha}(\text{Hg}, \Gamma, \text{IR}_{\alpha})$ and $e_{\alpha}(\text{X}, \Gamma, \text{IR}_{\alpha})$ for Hg and X atoms (X=Te, Se, and, S), while $e_{\alpha}(\text{Hg}, \Gamma, \text{IR}_{\beta}) = 0$ and $e_{\alpha}(\text{X}, \Gamma, \text{IR}_{\beta}) = 0$ for $\alpha \neq \beta$. For example, the eigenvectors of IR_x mode are $e_x(\text{Hg}, \Gamma, \text{IR}_x) = 0.79$ and $e_x(\text{Te}, \Gamma, \text{IR}_x) = -0.60$ for HgTe, $e_x(\text{Hg}, \Gamma, \text{IR}_x) = 0.37$ and $e_x(\text{Se}, \Gamma, \text{IR}_x) = -0.93$ for HgSe, and $e_x(\text{Hg}, \Gamma, \text{IR}_x) = 0.16$ and $e_x(\text{S}, \Gamma, \text{IR}_x) = -0.99$ for HgS. We estimated the Born effective charge of HgX in its insulating phase under the epitaxial strain [10]. The detailed parameters for the model Hamiltonian, achieved from DFT calculation, are summarized in Table S1.

In the main text, we investigated the nonlinear phonon interaction in the primitive unit

cell and topological properties in the cubic cell. Figure S1(a) shows the lattice vectors in the primitive unit cell (blue arrows) and related Cartesian vectors (red arrows, \hat{x}_p , \hat{y}_p , and \hat{z}_p). Figure S1(b) reveals the lattice vectors (blue arrows) in cubic cell and the corresponding Cartesian vectors of the primitive unit cell (red arrows, $\hat{x}'_p = \hat{x}_p$, $\hat{y}'_p = \hat{y}_p$, and $\hat{z}'_p = \hat{z}_p$) as shown in Fig. S1(a). These Cartesian vectors of primitive cell converted into cubic cell can be expressed in terms of the lattice vectors in the cubic cell, as follows: $\hat{x}'_p = 1/\sqrt{2}\hat{a}_c + 1/\sqrt{2}\hat{b}_c$, $\hat{y}'_p = -1/\sqrt{6}\hat{a}_c + 1/\sqrt{6}\hat{b}_c - 2\sqrt{6}\hat{c}_c$, and $\hat{z}'_p = -1/\sqrt{3}\hat{a}_c + 1/\sqrt{3}\hat{b}_c + 1/\sqrt{3}\hat{c}_c$ when \hat{a}_c , and \hat{x}'_p are the lattice vectors in the cubic cell and the Cartesian vector of the primitive cell into the cubic cell, respectively. The conversion could be verified by comparing primitive and cubic geometries. For example, \hat{x}_p and \hat{x}'_p are the directions along with the Hg atom and its nearest neighbor Hg atom that is bound with the same Te atom, and \hat{z}_p and \hat{z}'_p is the direction along with the Hg-Te bond. Once we decided the Cartesian vector \hat{x}'_p in the cubic cell, the orthogonal condition between Cartesian vectors provides the \hat{y}'_p and \hat{z}'_p . This conversion makes it possible to transform the motion of IR phonon modes in the primitive cell into the cubic cell.

Electronic structure of optimized geometry in bulk HgTe, HgSe, and HgS

We investigated the electronic structure of bulk HgTe, HgSe, and β -HgS through the density functional theory calculation using the VASP package. As shown in Fig. S2, with the PBE functional, HgTe and HgSe exhibit the metallic band structure with four degenerated states at Γ , while β -HgS has a small energy gap (0.1 eV) at Γ point [11]. Through the AIMD simulation in β -HgS, HgSe, and HgTe, we found that the nonlinear phonon interaction and emergence of Weyl points in these structures are robust regardless of the bandgap at the Γ point.

Plasmon frequency in bulk HgTe

We estimated the plasmon frequency in bulk HgTe using the Drude model. The frequency of plasmon in the Drude model is defined as $\omega_p = \sqrt{\frac{ne^2}{\epsilon_0 m_e}}$, when n , e , ϵ_0 and m_e are carrier density, electron charge, vacuum permittivity and mass of electron, respectively. In the study of M. Grynberg *etal.*, they reported the carrier density and effect of plasmon on

the reflectivity in bulk HgTe at various temperature [9]. At the low temperature (4.2 K), the lowest electron carrier concentration $6 \times 10^{15} \text{ cm}^{-3}$ is observed from the Hall measurement. This electron carrier concentration in bulk HgTe leads to the plasmon frequency 0.53 THz. As a result, negligible hybridization between plasmon and longitudinal optical mode is expected. This report indicates that plasmon's contribution can be neglected at low temperatures.

Meta-stable geometry induced by THz pulse and role of dissipation

In Fig. S3, THz field-induced atomic displacement along the IR mode is evaluated for Hg and Te atoms with various field strengths. With light pulse with $\omega = 2.6 \text{ THz}$, the dynamics of HgTe were achieved with various conditions, as shown in Fig. S3. The meta-stable state in HgTe, which shows atomic distortion along the Q_{ind} mode, was evaluated within a few picoseconds. Notably, the amplitude of this displacement relies on the applied field strength. On the other hand, the fast decay of meta-stable state was found in HgSe and β -HgS as shown in Figs. S3b and S3c. This behavior originates from the frequent phonon-phonon scattering with the larger displaced Q_x and Q_{ind} modes in HgSe and β -HgS. Because the normal coordinate contains the factor of effective mass (M_{eff}), the same amplitude of normal coordinate in β -HgS is the longer atomic displacement with factor of $M_{\text{eff}}^{\text{HgTe}}/M_{\text{eff}}^{\beta\text{-HgS}}$ comparing with HgTe case. In other words, the lighter atom shows the larger atomic displacement under a given electric field strength that can lead to the higher anharmonic coupling. Through the Model simulation, we verified the HgSe and β -HgS have higher nonlinear phonon coupling strength, as shown in Table 2. Figure S4 shows the time-dependent profile of atomic displacement from their equilibrium position in the Cartesian coordinate. The atomic displacement of the S atom shows a much larger amplitude with $E = 700 \text{ kV/cm}$ than those of Te and Se atoms under the same pumping strength.

Nonlinear Phonon interaction in the simplified model

We investigated the simplified model for the nonlinear phonon interaction in HgTe, HgSe, and β -HgS. The equation of motion for the Q_x and Q_{ind} modes are given as follows:

$$\begin{aligned}
\ddot{Q}_x + \gamma\dot{Q}_x + \Omega^2 Q_x &= -2k_{nl}Q_x Q_{ind} + Z^* E(t), \\
\ddot{Q}_{ind} + \gamma\dot{Q}_{ind} + \Omega^2 Q_{ind} &= -k_{nl}Q_x^2,
\end{aligned}
\tag{2}$$

when Ω , k_{nl} , and Z^* are phonon frequency, nonlinear phonon coupling coefficient, and Born effective charge, respectively [12]. These parameters for the HgTe, HgSe, and β -HgS are summarized in Table S2. We found that this effective classic model provides consistent dynamics between Q_x and Q_{ind} modes without dissipation ($\gamma = 0.0$ THz) as that from our AIMD simulation shown in the main text (see Fig. 2). By applying the THz field pulse, the initially displaced Q_x mode excites the Q_{ind} mode through the nonlinear phonon interaction. As shown in Fig. S5, an effective classic model with nonlinear phonon interactions provides consistent results about the excitation of Q_{ind} with that from the AIMD simulation.

The model simulations reproduce the THz field-induced meta-stable geometries in the family of HgTe that are simulated from AIMD calculations. We applied the same THz field pulse in our model simulation as follows: $\mathbf{E}(\mathbf{t}) = \mathbf{E}_0 \sin(\omega(\mathbf{t} - \mathbf{t}_0))e^{-(\mathbf{t}-\mathbf{t}_0)^2/\sigma^2} \hat{\mathbf{x}}$. It describes that the THz field pulse excites the Q_x directly and Q_{ind} through the nonlinear phonon interaction without dissipation ($\gamma = 0.0$ THz), as shown in Fig. S6. Overall, the Q_x oscillates around the equilibrium position, and its amplitude is increased with the increase of THz field strength. The oscillation of Q_{ind} shifts its time-average position, and this displacement relies on the THz field strength. We found that the maximum amplitudes of Q_x and Q_{ind} induced by THz field pumping are consistent with that from our AIMD simulation at the low intensity ($E < 1.0$ MV/cm) as shown in Fig. S3 and Fig. 2d in the main text. This result indicates that our newly developed AIMD methods complemented the model simulations at a low field strength range.

However, with high field strength ($E = 1.5$ MV/cm), the meta-stable state from the model simulation shows faster divergence than that from AIMD simulation, as depicted in Fig. S3. It originates from the absence of a dissipation channel in the model simulations. As shown in Fig. S7, we investigated the time-dependent Q_x and Q_{ind} induced by $E = 1.0$ MV/cm THz pulse with various dissipation ratios. For the dissipation effect in the system, we considered a fractional damping term ($\gamma\dot{Q}$). The higher dissipation ratio decreases the amplitudes of Q_x and Q_{ind} . For instance, the higher dissipation ratio ($\gamma = 0.06$ THz) leads to a quick

decay into the ground state within a few picoseconds. Compared with AIMD results, the model simulation with the dissipation ratio $\gamma = 0.005$ THz provides similar dynamics for the HgTe. These results reveal that our AIMD simulation describes effective dissipation during the THz field-induced dynamics as the model simulation with fractional dissipation.

In addition, we also investigated light-induced dynamics AIMD simulation with a thermostat. We found that the ionic motion constrained by the thermostat degrades the formation of meta-stable geometry in HgTe. Without a thermostat, the THz-induced averaged atomic displacement is evaluated with $E = 1.5$ MV/cm, as shown in Fig. S8a. The oscillating field induces the oscillation of Hg and Te with amplitude of 0.1 Å and 0.2 Å, respectively. With the thermostat at 100 K, on the other hand, the amplitude of excited atomic displacement degraded significantly, as shown in Fig. S8b. This suppressed THz-induced excitation of IR mode leads to the negligible meta-stable geometry. This result indicates that the AIMD with a thermostat is inappropriate for light-induced non-equilibrium dynamics.

Weyl points in the Fermi arc surface states

The distorted geometry along the \mathbf{Q}_{ind} results in the emergency of the Weyl points in bulk HgTe. The Fermi arc surface states for the distorted lattice with $\mathbf{Q}_{ind} = 0.5 \text{ Å}\sqrt{\mu}$ are shown in Fig. S8. The Weyl points induced by THz field pumping locate at $W_1^+ = (k_x, k_y, k_z)$, $W_2^+ = (-k_x, -k_y, -k_z)$, $W_1^- = (-k_y, -k_x, k_z)$, and $W_2^- = (k_y, k_x, -k_z)$, but in which $k_x = -33.6 \text{ mÅ}^{-1}$, $k_y = 22.4 \text{ mÅ}^{-1}$, and $k_z = 35.3 \text{ mÅ}^{-1}$. We also evaluated the Fermi arc surface states for HgSe and HgS under THz field pumping. The results are shown in Fig. S9 and S10. Due to the same crystal symmetries, the Weyl points in HgSe and β -HgS driven by the THz light still stay at W_1^+ , W_2^+ , W_1^- , and W_2^- but with different k values. For the HgSe with $\mathbf{Q}_{ind} = 0.5 \text{ Å}\sqrt{\mu}$, $k_x = -0.49 \text{ mÅ}^{-1}$, $k_y = 31.1 \text{ mÅ}^{-1}$, and $k_z = 36.9 \text{ mÅ}^{-1}$. And for β -HgS with $\mathbf{Q}_{ind} = 0.5 \text{ Å}\sqrt{\mu}$, $k_x = 26.4 \text{ mÅ}^{-1}$, $k_y = -1.75 \text{ mÅ}^{-1}$, and $k_z = 31.1 \text{ mÅ}^{-1}$.

Symmetry analysis and Berry curvature dipole

Our study evaluated the Berry curvature and Berry curvature dipole from the tight-binding model constructed from the maximally localized Wannier functions [5]. As shown in Fig. S11, the non-zero Berry curvature at the Fermi level is found near the Weyl points.

The Berry curvature can be evaluated from derivative of Berry connection as follows: $\Omega^k = \epsilon_{ijk}(\partial_i \mathbf{A}_j - \partial_j \mathbf{A}_i)$, where A_i is the Berry connection. The Berry curvature dipole (\mathbf{D}_{ab}) can be written in terms of Berry curvature as follows: $\mathbf{D}_{ab} = -\int \frac{d^3\mathbf{k}}{(2\pi)^3} \sum_{\mathbf{n}} \mathbf{v}^{\mathbf{n}\mathbf{k}} \Omega_{\mathbf{n}\mathbf{k}}^b \frac{\partial f_{\mathbf{n}\mathbf{k}}^0}{\partial E_{\mathbf{n}\mathbf{k}}}$ when v_a , f^0 and E_{nk} are the Fermi velocity, the Fermi-Dirac occupation and the eigenvalue of the n^{th} Bloch state at the k point, respectively [13]. Without any symmetric conditions, the trace of the Berry curvature dipole should be zero ($\mathbf{D}_{xx} + \mathbf{D}_{yy} + \mathbf{D}_{zz} = \mathbf{0}$).

Here, we analyzed the components of the Berry curvature dipole under the symmetry analysis. First, we investigated the Berry curvature dipole of geometrically optimized bulk HgTe ($F\bar{4}3m$) in terms of symmetry analysis. In the symmetric operation Group $F\bar{4}3m$ No.216, we had the three operations C_{2z} , C_{2x} , C_{2y} for two-fold symmetry, and single operations C_3 for three-fold symmetry. The C_{2z} operator gives the transformation as follows:

$$\begin{aligned}
C_{2z} : (x, y, z) &\rightarrow (-x, -y, z) \\
C_{2z} : (v_x, v_y, v_z) &\rightarrow (-v_x, -v_y, v_z) \\
C_{2z} : \Omega^i &= \epsilon_{ijk}(\partial_j A_k - \partial_k A_j) \rightarrow -\Omega^i = \epsilon_{ijk}(-\partial_j A_k + \partial_k A_j) \\
C_{2z} : (\Omega^x, \Omega^y, \Omega^z) &\rightarrow (-\Omega^x, -\Omega^y, \Omega^z)
\end{aligned} \tag{3}$$

This symmetry operation on the Berry curvature guarantees the symmetry relation of the Berry curvature dipole as follows:

$$\begin{aligned}
C_{2z} : (D_{xx}, D_{yy}, D_{zz}) &\rightarrow (D_{xx}, D_{yy}, D_{zz}) \\
C_{2z} : (D_{xy}, D_{yz}) &\rightarrow (D_{xy}, D_{yz}) \\
C_{2z} : (D_{xz}, D_{yz}, D_{zy}) &\rightarrow (-D_{xz}, -D_{yz}, -D_{zy}) = 0
\end{aligned} \tag{4}$$

Similar to the analysis under the C_{2z} operator, we could get the same results for C_{2x} and C_{2y} operators, we find that only diagonal terms survive.

In the C_3 rotation symmetry, the position, Fermi velocity, and the Berry curvature con-

strained by the symmetry operation of C_3 become

$$\begin{aligned}
C_3 : (x, y, z) &\rightarrow (z, x, y) \\
C_3 : (v_x, v_y, v_z) &\rightarrow (v_z, v_x, v_y) \\
C_3 : \Omega^i = \epsilon_{ijk}(\partial_j A_k - \partial_k A_j) &\rightarrow \Omega^k = \epsilon_{ijk}(-\partial_i A_j + \partial_j A_i) \\
C_3 : (\Omega^x, \Omega^y, \Omega^z) &\rightarrow (\Omega^z, \Omega^x, \Omega^y)
\end{aligned} \tag{5}$$

Furthermore, we could also derive the C_3 symmetry operation on the Berry curvature dipole as follows:

$$C_3 : (D_{xx}, D_{yy}, D_{zz}) \rightarrow (D_{zz}, D_{xx}, D_{yy}) \tag{6}$$

Guaranteed by these symmetry conditions, we find the zero Berry curvature dipole ($D_{xx} = D_{yy} = D_{zz} = 0$).

We investigated the Berry curvature dipole constrained by the crystal symmetry in the bulk HgTe with the THz light-induced distortion. In the distorted geometry of HgTe, there is only one mirror symmetry $m_{(110)}$, which guarantees:

$$\begin{aligned}
m_{(110)} : (x, y, z) &\rightarrow (-y, -x, z) \\
m_{(110)} : (v_x, v_y, v_z) &\rightarrow (-v_y, -v_x, v_z) \\
m_{(110)} : \Omega^x = \partial_y A_z - \partial_z A_y &\rightarrow \Omega^y = -\partial_x A_z + \partial_z A_x \\
m_{(110)} : \Omega^z = \partial_x A_y - \partial_y A_x &\rightarrow -\Omega^z = \partial_y A_z - \partial_x A_y \\
m_{(110)} : (\Omega^x, \Omega^y, \Omega^z) &\rightarrow (\Omega^z, \Omega^x, \Omega^y) \\
m_{(110)} : (\Omega^x, \Omega^y, \Omega^z) &\rightarrow (\Omega^y, \Omega^x, -\Omega^z)
\end{aligned} \tag{7}$$

Then we could find the Berry curvature dipole under mirror symmetry:

$$m_{(110)} : (D_{xx}, D_{yy}, D_{zz}) \rightarrow (-D_{yy}, -D_{xx}, -D_{zz}) \tag{8}$$

Due to the zero trace of Berry curvature dipole ($\sum_{i=x,y,z} D_{ii} = 0$), we could find:

$$D_{xx} + D_{yy} + D_{zz} = -D_{yy} + D_{yy} + D_{zz} = D_{zz} = 0 \tag{9}$$

and

$$D_{xx} = -D_{yy} \quad (10)$$

The results from the symmetry analysis are consistent with the calculated results shown in Fig. 4 of the main text.

Screening effect by static electric field on HgTe

In our proposal shown in the main text, we need to account for the time-dependent external electric field $E(t)$ in three-dimensional periodic boundary conditions. This means we can use the Lorentz force with Born effective charge of bulk HgTe to describe how the external electric field affects the system. To obtain the Born effective charge Z_{τ}^{bec} , we applied the linear response perturbation theory to bulk HgTe system with the ground geometry. Then we calculated the forces $F_{\tau}^{Lor} = -dE_0^{KS}/d\tau + Z_{\tau}^{bec}E(t)$ with a given electric field $E(t)$, where $-dE_0^{KS}/d\tau$ is Hellman-Feynman forces from the Kohn-Sham total energy E_0^{KS} without the contribution from the external electric field. In HgTe, the Born effective charges of the Hg atom and Te atom are with opposite signs ($Z_{Hg}^{bec} \sim -Z_{Te}^{bec}$), so the force direction is opposite for Hg atom and Te atom as shown in Fig. S13(a). This approach is usually employed in *ab initio*-based molecular dynamics simulation [8, 14]. In this approach, the screening effect induced by the external electric field is not considered. The screening effect from the intrinsic semi-metallic HgTe has been fully taken into account.

On the other hand, because the bulk HgTe is a semimetal, the screening effect induced by the external electric field could affect the dynamics in principle. To estimate the screening effect in HgTe, we applied the static electric field to the thin film of HgTe, and then directly calculated the induced force from the *ab initio* DFT calculations. We named this approach as the length gauge (LG) method. Because the calculated force is obtained from self-consistent DFT calculations, including the external electric field, the corresponding screening effect is fully considered here.

In detail, as shown in Fig. S13(a) and (b), we use a (001) slab model of HgTe with the thickness of 16.8 Å to simulate the case under an external electric field. A vacuum layer with 23.2 Å is added along the z direction between the neighboring HgTe slabs. The three-dimensional periodic boundary conditions are still used in our calculations. The length gauge method allows for the description of electron and ion interactions under the external electric

fields by transforming the static constant electric field E into a scalar potential term $V(r)$. This potential along the z -axis can be expressed as $V(z) = -Ez\hat{z}$, then the Kohn-Sham Hamiltonian becomes $H^{KS} = H_0^{KS} + V(z)$, where H_0^{KS} is Kohn-Sham Hamiltonian without a static electric field with the energy of E_0^{KS} . We could do the self-consistent calculation to obtain the Kohn-Sham energy. Then the force can be calculated by $F_\tau^{LG} = -dE^{KS}/d\tau$ where E^{KS} in length gauge is the energy of Kohn-Sham Hamiltonian H^{KS} . Due to the periodic boundary conditions, the scalar potential must also have periodicity, which can be achieved using a saw-tooth-type scalar potential, as shown in Fig. S13(b). The scalar potential for $+E$ field is employed in the range of $0.0 < z < 0.9c_0$ while a decreasing scalar potential for $-E$ field is used in the range of $0.9c_0 < z < c_0$, in which c_0 is the lattice value along z direction in the slab model [15]. This approach directly evaluates electron-ion interactions under the external static electric field, including the screening effect.

To apply the saw-tooth-type electric field, we utilize the (001) HgTe slab with the Te termination, which is displayed in Fig. S13(c). We first compare the electronic structures between the (001) HgTe slab with Te termination and bulk HgTe and determine if the slab geometry is thick enough to reproduce the electronic structure for the bulk state. The slab model has been fully relaxed without including the external electric field. As shown in Fig. S13(d), the density of states between the slab and bulk HgTe exhibit similar trends, such as a lower density of states at the Fermi level and peak states near energy levels of -2 and 2 eV. This result suggests that the (001) HgTe slab with Te termination is thick enough to simulate the electronic structure of bulk HgTe. We also found that the Born effective charges of Hg atom and Te atom for the z -direction are reduced in the slab model as $Z_{Hg}^{bec} = 0.35e$ and $Z_{Te}^{bec} = -0.35e$.

We evaluate the screening effect on the slab geometry by comparing the Lorentz-type force with that calculated from the length gauge method. Here, Figure S13(e) shows the average and deviation values for the calculated forces on two types of ions in the slab geometry. If the applied electric field strength is below 0.5 MV/cm, the calculated forces on Hg atom and Te atom are almost the same for the two methods. This result suggests that under the electric field $E < 0.5$ MV/cm, the induced screening effect is not significant. On the other hand, once the electric field strength is extremely large, such as $E > 1.3$ MV/cm, we can observe the difference between the calculated forces from Lorentz-type and length gauge methods. Even under the maximal value for the used electric field strength in our paper

(see Fig. 2 in the main text), the difference ratio $(F_{\tau}^{Lor} - F_{\tau}^{LG})/F_{\tau}^{Lor}$ is about 12.2%. To conclude, we believe that the force calculated from Lorentz-type is good enough to describe the effect induced by the external electric field for bulk HgTe. The screening effect induced by the external electric field does exist, but its influence is limited for bulk HgTe, the main conclusions shown in our paper will not be changed once we consider the screening effect.

Nonlinear phonon interaction; detail and examples

The nonlinear phonon interaction has recently been highlighted as a key mechanism for various light-induced phenomena [5, 16–20]. When the strong THz-field pulse with a given frequency is applied to the material, the infrared active (IR) phonon mode could be resonantly excited, and the oscillation amplitude Q_{IR} will be largely enhanced. At this condition, the excited IR phonon mode in the anharmonic range can affect the other phonon modes via the nonlinear phonon interaction. As an example, if the nonlinear phonon interaction between the IR phonon and a Raman phonon has the form of $k'Q_{IR}^2Q_R$ in which Q_R is its oscillation amplitude for Raman phonon mode and k' is the coupling coefficient, the largely displaced IR-active phonon mode can modify the potential energy surface for Raman phonon mode as $(\omega_R^2Q_R^2 + k'Q_{IR}^2Q_R)$, where ω_R is the frequency of the Raman phonon mode. In such a case, the minimum position around which the Raman phonon is oscillating will be shifted, and the displacement is proportional to the value of Q_{IR}^2 that can be enhanced with increasing the strength of THz laser field. The lattice distortion resulting from nonlinear phonon interactions has a comparable impact to internally applied strain on the lattice, enabling the alteration of material properties, such as inducing a phase transition.

Effect of static electric field on HgTe

Our study demonstrates the topological phase transition in HgTe via nonlinear phononics by applying an external THz laser field. Unlike the light-driven case in which the THz pulse can be applied to the bulk sample effectively, the large static electric field can only be applied to the thin-film sample or can affect the surface of the bulk sample in the experiment. If the thickness of the HgTe thin film is small enough, the two-dimensional (2D) quantum well states will dominate the electronic properties around the Fermi level. With the change of

the thickness for HgTe, a topological phase transition can be achieved and the 2D quantum spin Hall (QSH) effect can be observed. In fact, the first QSH effect is proposed and realized in the strained HgTe thin film with a suitable thickness [21, 22]. In such case, if a static electric field is applied, the quantum well states around the Fermi level will be modified, and we expect to observe a topological phase transition for HgTe thin film [23].

If the thickness of the HgTe film is not too small and its electronic property is close to that of the bulk state, the applied static electric field should not be too large. To estimate the effect of the static field on the lattice distortion for the HgTe thin film, we relaxed the atomic positions of (001) HgTe thin film under the static electric field. We performed the same method that is used in length gauge calculation as shown in Fig. S13. For example, the static electric field with the value of 0.5 MV/cm displaces the atomic positions of Hg and Te atoms as $\mathbf{Q}_{\text{Hg}} = 0.22m\text{\AA}$ and $\mathbf{Q}_{\text{Te}} = -0.26m\text{\AA}$, respectively. These values are much smaller than those induced by nonlinear phononic with the same field strength. Such small atomic displacement could break the intrinsic lattice symmetry of HgTe, but because the shiftiness is too small, we expect the negligible separation of Weyl points for the observation, as shown in Fig. 3(b) in the main text.

On the other hand, applying the static electric field with the magnitude of MV/cm on the semi-metallic bulk HgTe causes a large current flow because of the induced asymmetric carrier distribution near the Fermi level, which should dominate the physical measurement in such a condition. While, in our proposed light-induced dynamics via nonlinear phononics, the direct interaction for the THz light with the electron degree of freedom in HgTe bulk is not important because of a large difference between the frequency of THz light and the Drude frequency in HgTe bulk. Even if we do not consider the screening effect and treat the HgTe as a dielectric material, a few MV/cm static field is large enough to break down the bulk sample [24]. Such a side effect might limit the observation of any physical effect proposed in HgTe induced by the static electric field.

For the application of the extended *ab initio* molecular dynamics (AIMD) method that is proposed in this work, we believe it is only suitable for the insulating system or the semimetal with almost zero density of state (DOS) at the Fermi level, such as bulk HgTe. For a metallic system with a large DOS at the Fermi level, we must seriously consider the screening effect induced by the external electric field. To demonstrate such an effect, we add the electron and hole to HgTe slab model artificially, apply a saw-tooth-type potential

to the sample (see Fig. R1(d) for details), and calculate the field-induced force on Hg and Te atoms in the framework of DFT. As shown in Fig. S13 of the supplementary material in the revised manuscript and the previous response letter, the Lorentz-type force is almost the same as that calculated from the length gauge field method for the intrinsic HgTe slab. Thus, herein, we just apply the length gauge field method to these slab models with different electron and hole doping.

We additionally investigate the calculated forces on each atom in the HgTe slab model with electron doping and hole doping to demonstrate that the screening effect induced by an external electric field is important for metallic systems. The length gauge field method is applied to HgTe slab models. The calculated results are shown in Fig. S14. Once we dope more electrons or holes to make the HgTe slab metallic, the calculated forces are very different from the case without doping. The pristine HgTe slab has asymmetric DOS distribution around the Fermi level as shown in Fig. S14(b). When the same value of charges is added artificially, the HgTe slab with hole doping has a much higher DOS at the Fermi level compared with the case with electron doping as shown in Figs. S14(a) and (e). Correspondingly, we can find a more noteworthy change in the calculated force induced by hole doping in contrast to the case with electron doping as shown in Figs. S14(c) and (f). Our calculated results clearly show that if a system is more metallic, the forces induced by the external electric field exhibit a more dramatic reduction compared with the calculated Lorentz force based on the Born-effective charges.

Phonon dispersion in bulk HgTe family

We evaluated the phonon dispersion for bulk HgTe and highlighted the TO modes with red lines as shown in Fig. S15(a). At the Γ point, the frequencies for TO and LO modes are evaluated as 3.5 THz and 3.96 THz, such difference originates from the LO-TO splitting [25]. Our calculated values are exactly the same as the experimental observations [9]. We also evaluate the phonon dispersion for bulk HgSe, and β -HgS as shown in Fig. S15(b) and (c).

* dongbin.shin@mpsd.mpg.de

† angel.rubio@mpsd.mpg.de

[‡] peizhet@buaa.edu.cn

- [1] G. Kresse and D. Joubert, Phys. Rev. B **59**, 1758 (1998).
- [2] J. P. Perdew and A. Zunger, Phys. Rev. B **23**, 5048 (1981).
- [3] G. Pizzi, V. Vitale, R. Arita, S. Blgel, F. Freimuth, G. Granton, M. Gibertini, D. Gresch, C. Johnson, T. Koretsune, J. Ibaez-Azpiroz, H. Lee, J.-M. Lihm, D. Marchand, A. Marrazzo, Y. Mokrousov, J. I. Mustafa, Y. Nohara, Y. Nomura, L. Paulatto, S. Ponc, T. Ponweiser, J. Qiao, F. Thle, S. S. Tsirkin, M. Wierzbowska, N. Marzari, D. Vanderbilt, I. Souza, A. A. Mostofi, and J. R. Yates, J. Condens. Matter Phys. **32**, 165902 (2020).
- [4] Q. Wu, S. Zhang, H.-F. Song, M. Troyer, and A. A. Soluyanov, Comput. Phys. Commun. **224**, 405 (2018).
- [5] D. Shin, S. A. Sato, H. Hübener, U. D. Giovannini, N. Park, and A. Rubio, Npj Comput. Mater. **6**, 182 (2020).
- [6] P. Giannozzi *et al.*, J. Condens. Matter Phys. **29**, 465901 (2017).
- [7] I. Souza, J. Íñiguez, and D. Vanderbilt, Phys. Rev. B **69**, 085106 (2004).
- [8] M. Kozina, M. Fechner, P. Marsik, T. v. Driel, J. M. Glowina, C. Bernhard, M. Radovic, D. Zhu, S. Bonetti, U. Staub, and M. C. Hoffmann, Nat. Phys. **15**, 387 (2019).
- [9] M. Grynberg, R. L. Toullec, and M. Balkanski, Phys. Rev. B **9**, 517 (1972).
- [10] J. Ruan, S.-K. Jian, H. Yao, H. Zhang, S.-C. Zhang, and D. Xing, Nat. Commun. **7**, 11136 (2016).
- [11] A. Svane, N. E. Christensen, M. Cardona, A. N. Chantis, M. v. Schilfgaarde, and T. Kotani, Phys. Rev. B **84**, 205205 (2011).
- [12] A. Subedi, Phys. Rev. B **92**, 214303 (2015).
- [13] I. Sodemann and L. Fu, Phys. Rev. Lett. **115**, 216806 (2015).
- [14] X. Li, T. Qiu, J. Zhang, E. Baldini, J. Lu, A. M. Rappe, and K. A. Nelson, Science **364**, 1079 (2019).
- [15] J. Neugebauer and M. Scheffler, Phys. Rev. B **46**, 16067 (1992).
- [16] T. F. Nova, A. S. Disa, M. Fechner, and A. Cavalleri, Science **364**, 1075 (2019).
- [17] D. Shin, S. Latini, C. Schafer, S. A. Sato, E. Baldini, U. D. Giovannini, H. Hubener, and A. Rubio, Phys. Rev. Lett. **129**, 167401 (2022).
- [18] M. Först, C. Manzoni, S. Kaiser, Y. Tomioka, Y. Tokura, R. Merlin, and A. Cavalleri, Nat. Phys. **7**, 854 (2011).

- [19] R. Mankowsky, M. Först, and A. Cavalleri, Rep. Prog. Phys. **79**, 064503 (2016).
- [20] A. Subedi, A. Cavalleri, and A. Georges, Phys. Rev. B **89**, 220301 (2014).
- [21] B. A. Bernevig, T. L. Hughes, and S.-C. Zhang, Science **314**, 1757 (2006).
- [22] M. König, S. Wiedmann, C. Brüne, A. Roth, H. Buhmann, L. W. Molenkamp, X.-L. Qi, and S.-C. Zhang, Science **318**, 766 (2007).
- [23] P. Sengupta, T. Kubis, Y. Tan, M. Povolotskyi, and G. Klimeck, J. Appl. Phys. **114**, 043702 (2013).
- [24] A. Grigoriev, R. Sichel, H. N. Lee, E. C. Landahl, B. Adams, E. M. Dufresne, and P. G. Evans, Phys. Rev. Lett. **100**, 027604 (2008).
- [25] T. Ouyang and M. Hu, J. Appl. Phys. **117**, 245101 (2015).

TABLE S1. Computed parameters of HgTe, HgSe, and HgS structure from DFT calculations.

| | HgTe | HgSe | HgS |
|------------------------------------|--------|--------|--------|
| Lattice parameter (\AA) | | | |
| LDA | 4.559 | 4.301 | 4.122 |
| Atomic mass M (μ =amu) | | | |
| for Hg | 200.59 | 200.59 | 200.59 |
| for Te, Se, and S | 127.6 | 78.96 | 32.065 |
| Born effective charge Z (e) | | | |
| for Hg | 3.18 | 3.24 | 3.23 |
| for Te, Se, and S | -3.18 | -3.24 | -3.23 |
| Phonon frequency for IR mode (THz) | 3.5 | 4.55 | 5.4 |

TABLE S2. Parameters for the model simulation in HgTe, HgSe, and β -HgS.

| | HgTe | HgSe | HgS |
|--|------|------|------|
| Ω (THz/(2 π)) | 3.5 | 4.0 | 5.6 |
| k_{nl} (THz ² Å ⁻¹ μ ^{-1/2}) | 93 | 159 | 439 |
| Z^* (e μ ^{-1/2}) | 0.35 | 0.44 | 0.50 |

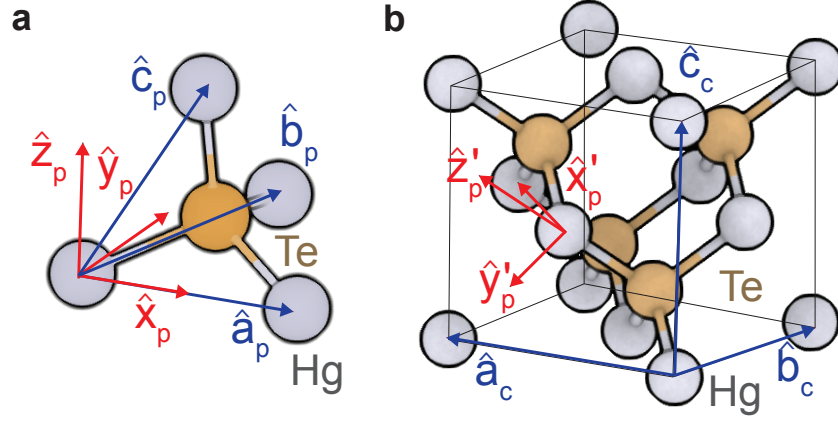


FIG. S1. **Conversion of Cartesian vectors in primitive lattice to cubic lattice.** **a**, Cartesian vectors (red) and lattice vectors (blue) in primitive lattice. **b**, Cartesian vectors of the primitive lattice (red) in cubic lattice and lattice vectors of cubic lattice.

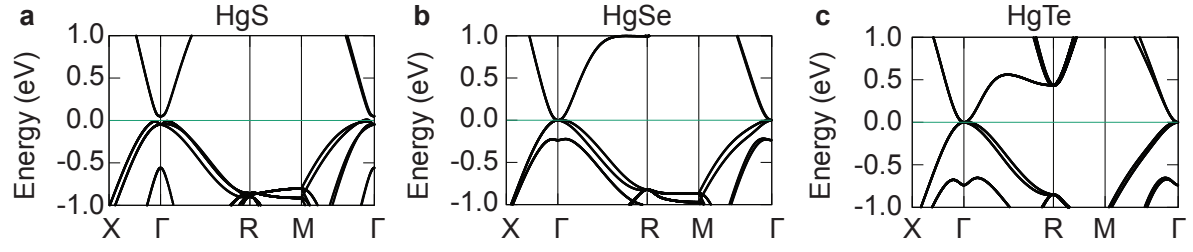


FIG. S2. **Band structure of HgS, HgSe, and HgTe.** a-c, Band structure calculated with PBE functional of (a) HgS, (b) HgSe, and (c) HgTe.

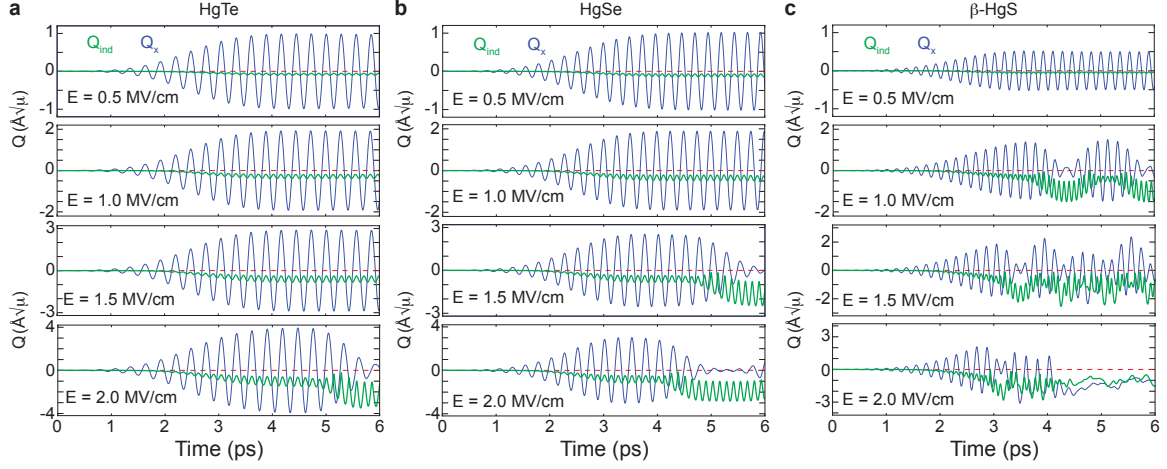


FIG. S3. **THz-field induced distorted geometry through the nonlinear phonon interaction through the *ab initio* MD simulation in normal coordinate.** **a**, Time profile of THz-field induced dynamics in bulk HgTe. **b**, Time profile of THz-field induced dynamics in bulk HgSe. **c**, Time profile of THz-field induced dynamics in bulk β -HgS.

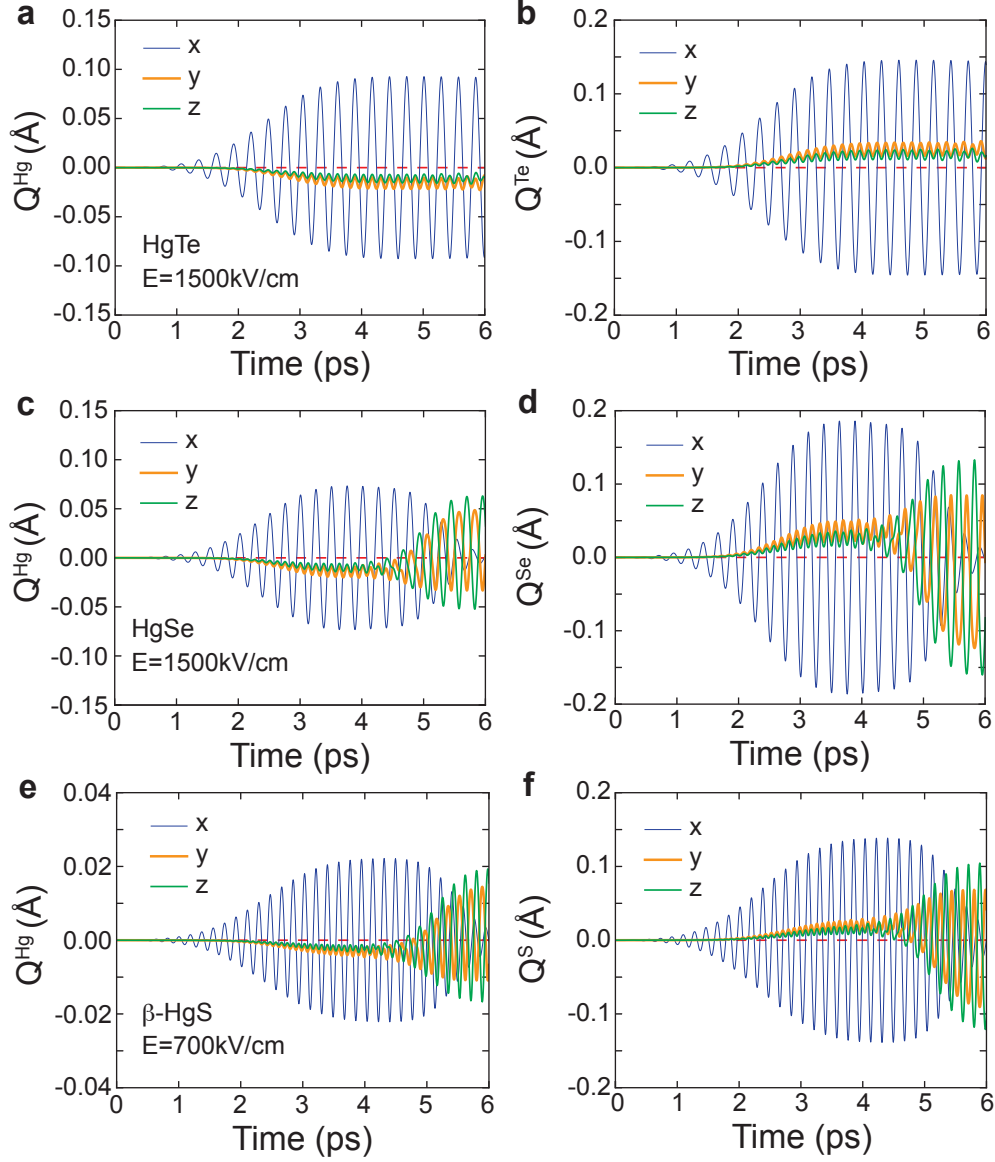


FIG. S4. THz-field induced distorted geometry through the nonlinear phonon interaction through the *ab initio* MD simulation in Cartesian coordinate. **a-b**, Time profile of THz-field induced dynamics for (a) Hg and (b) Te in bulk HgTe. **c-d**, Time profile of THz-field induced dynamics for (c) Hg and (d) Se in bulk HgSe. **e-f**, Time profile of THz-field induced dynamics for (e) Hg and (f) S in bulk β -HgS.

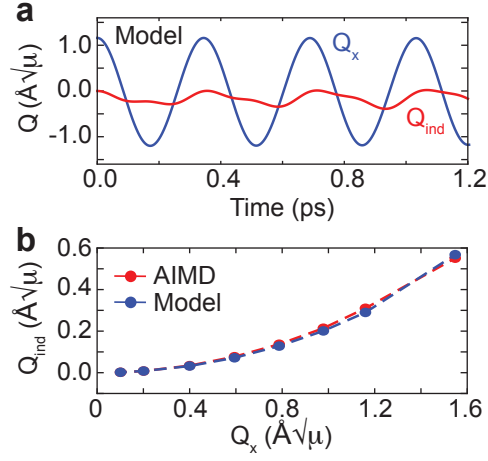


FIG. S5. **Nonlinear phonon interaction between IR modes in HgTe.** **a**, Time profile of nonlinear phonon dynamics evaluated with Model Hamiltonian simulation. **b**, Maximum amplitude of induced IR mode under the given initial IR_x mode.

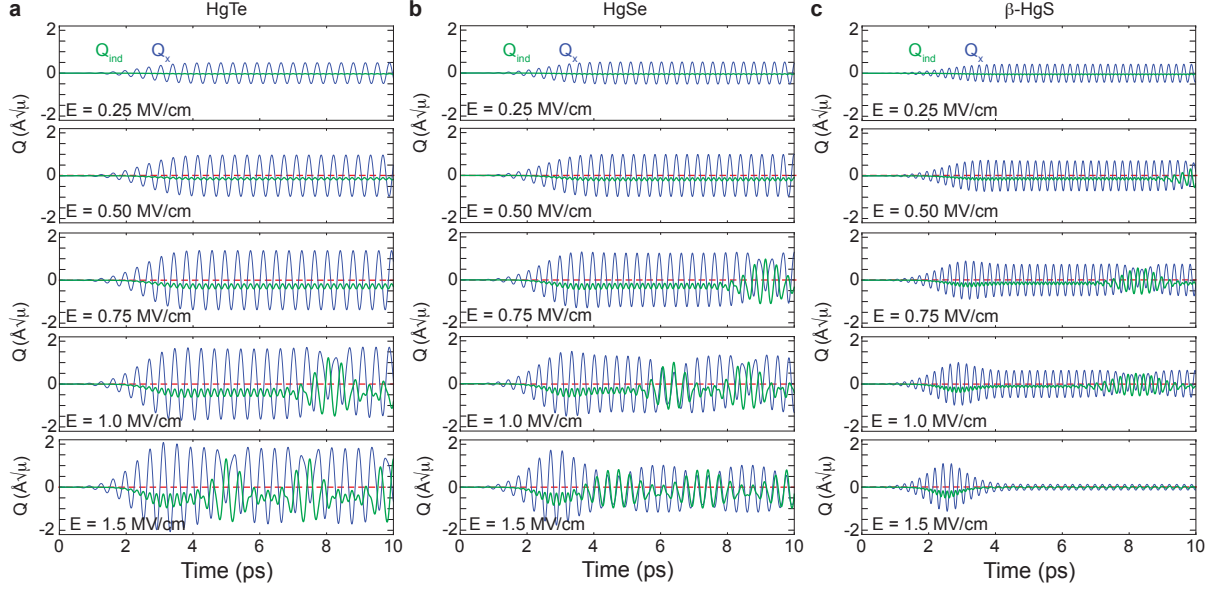


FIG. S6. **THz-induced dynamics in simplified model without fractional dissipation.** a-c, Time profile of THz-field induced dynamics in bulk (a) HgTe, (b) HgSe, and (c) β -HgS.

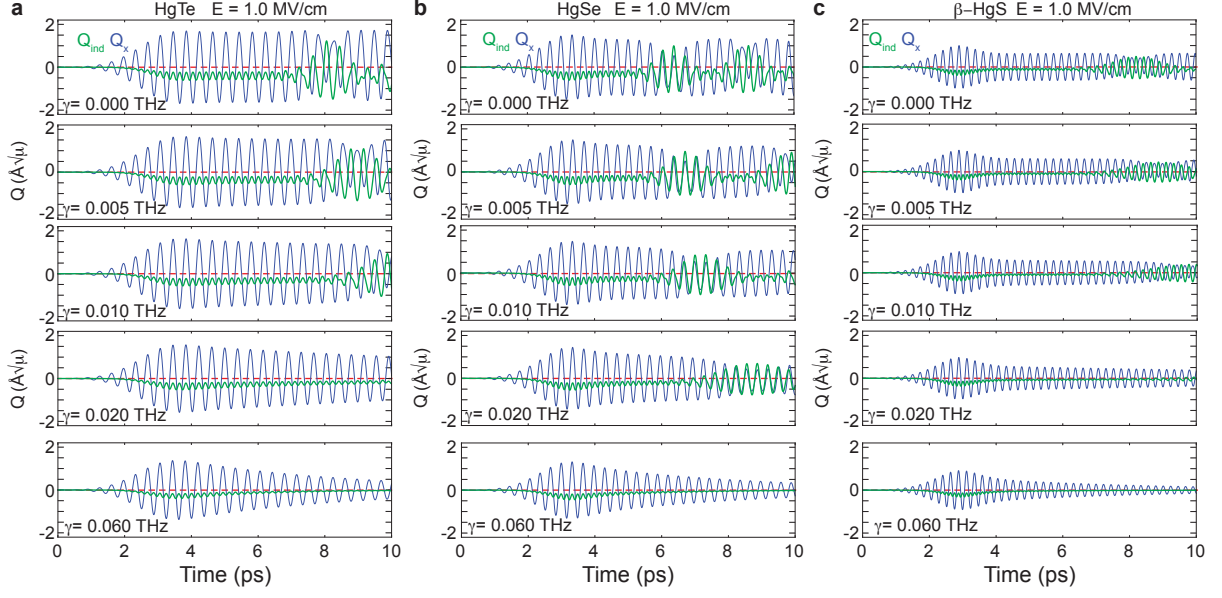


FIG. S7. **THz-induced dynamics in a simplified model with fractional dissipation.** **a-c**, Time profile of THz-field induced dynamics in bulk **(a)** HgTe, **(b)** HgSe, and **(c)** β -HgS with various dissipation ratios.

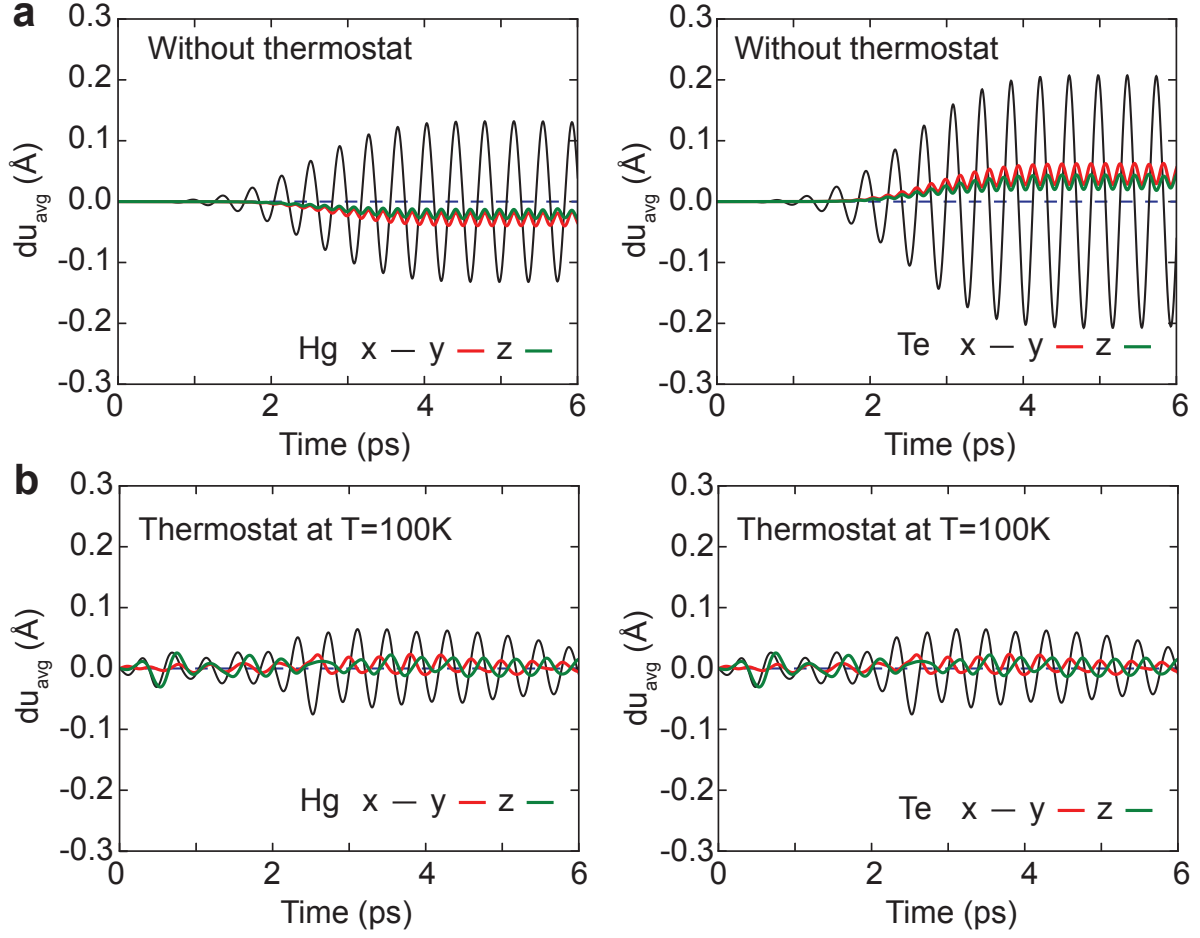


FIG. S8. **THz-induced dynamics with constrained condition.** **a-b**, Time-profile of averaged Hg and Te displacement (**a**) with, and (**b**) without thermostat.

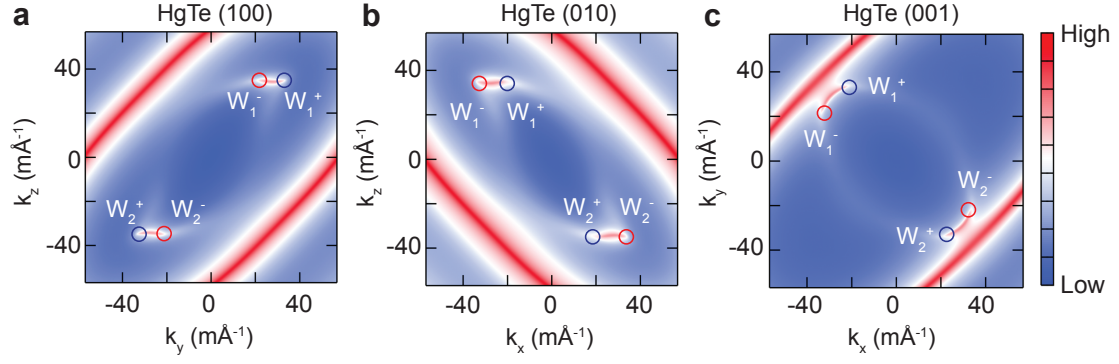


FIG. S9. **Fermi arc surface states of HgTe in the shifted equilibrium position by the nonlinear phononic interaction.** **a-c**, Fermi arc surface states in **(a)** (100), **(b)** (010), and **(c)** (001) surface with $Q_{ind} = 0.5 \text{ \AA}\sqrt{\mu}$ in HgTe.

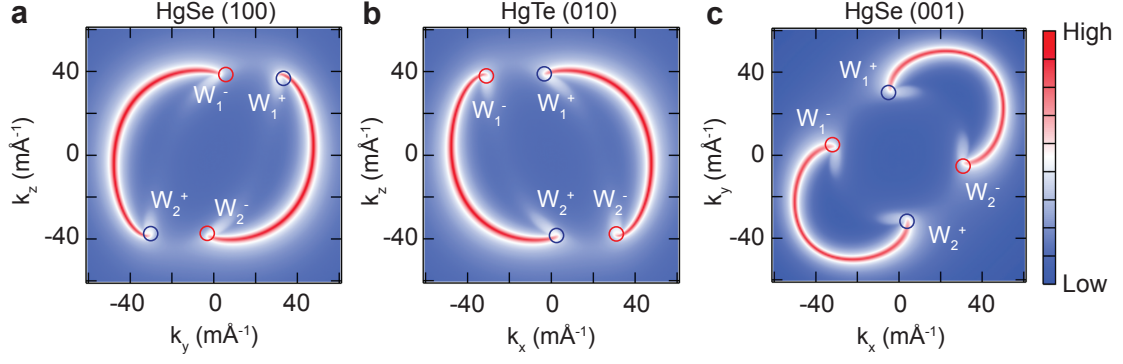


FIG. S10. **Fermi arc surface states of HgSe in the shifted equilibrium position by the nonlinear phononic interaction.** **a-c**, Fermi arc surface states in **(a)** (100), **(b)** (010), and **(c)** (001) surface with $Q_{ind} = 0.5 \text{ Å}\sqrt{\mu}$ in HgSe.

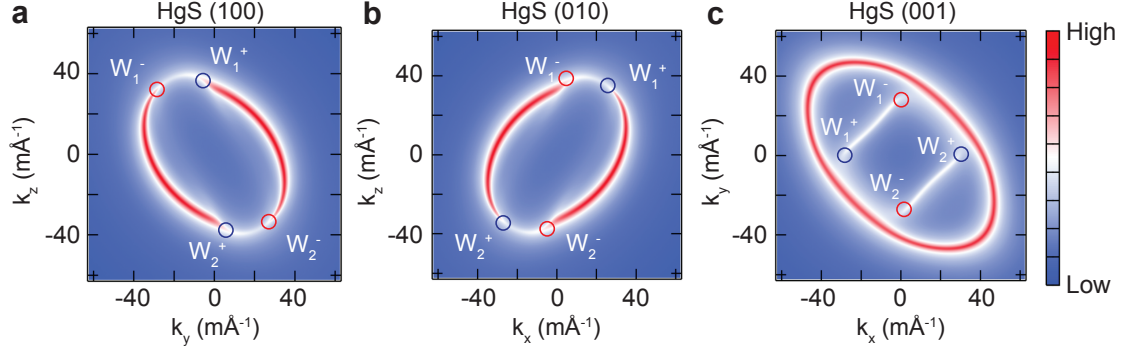


FIG. S11. **Fermi arc surface states of HgS in the shifted equilibrium position by the nonlinear phononic interaction.** **a-c**, Fermi arc surface states in **(a)** (100), **(b)** (010), and **(c)** (001) surface with $Q_{ind} = 0.5 \text{ \AA}\sqrt{\mu}$ in HgS.

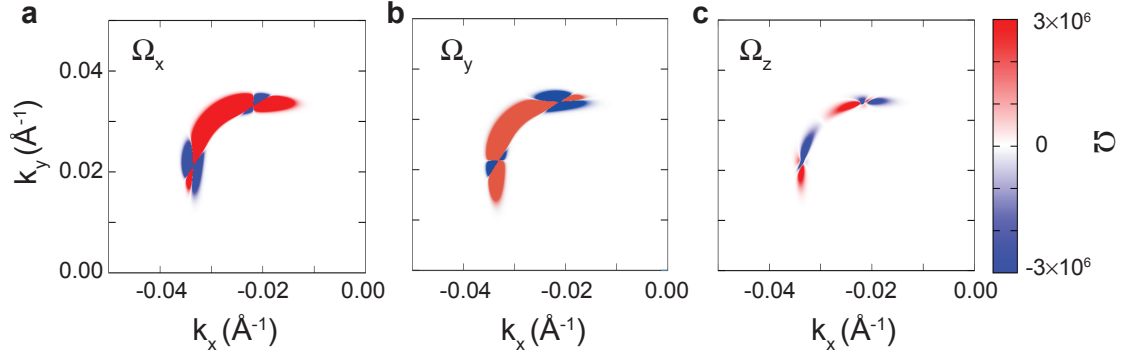


FIG. S12. **Berry curvature near Weyl points in the atomic distorted HgTe.** a-c, Berry curvature (a) Ω_x , (b) Ω_y , and (c) Ω_z at $k_z = 35.3 \text{ m\AA}^{-1}$ plane.

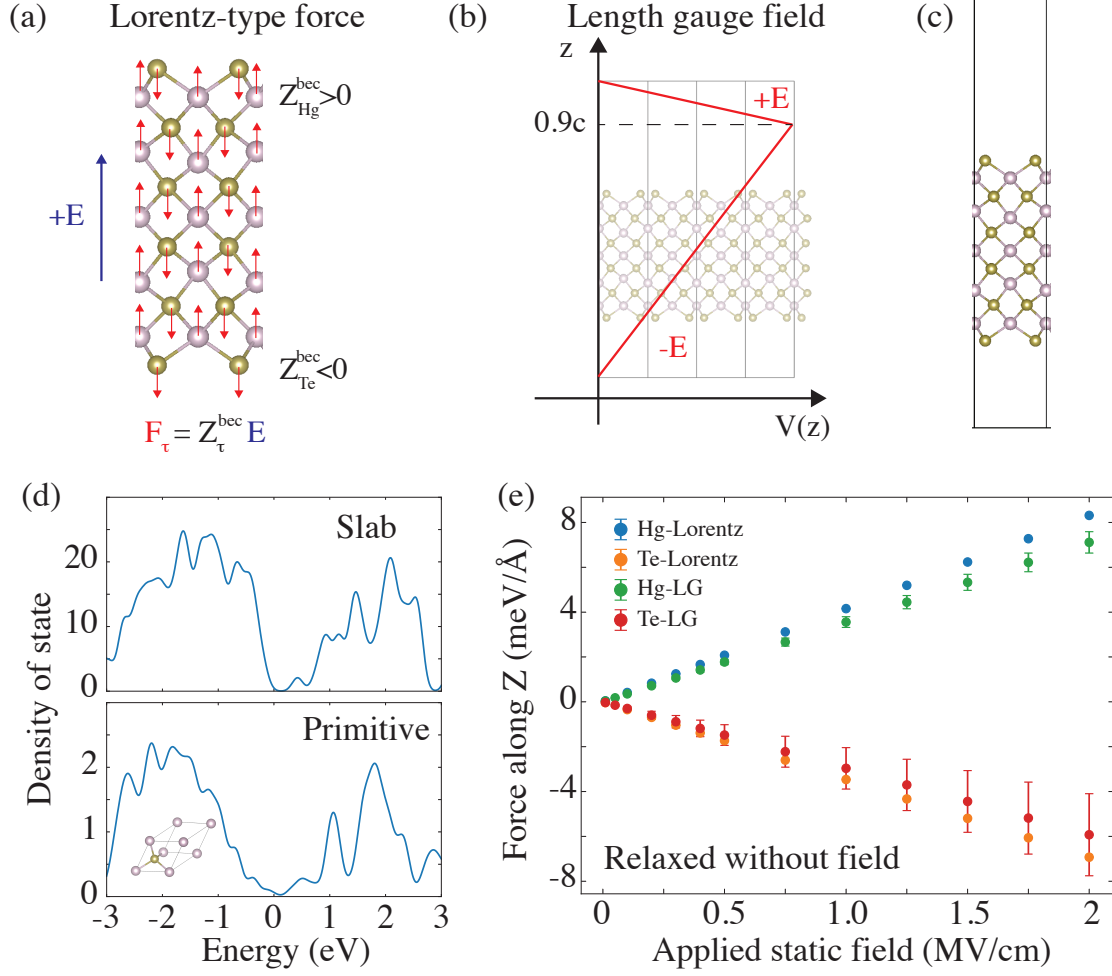


FIG. S13. Field-induced forces in the HgTe slab. Schematics of electric field-induced forces via (a) Lorentz-type force and (b) length gauge field. The red arrows in (a) demonstrate the force directions on each atom obtained from Lorentz-type force. The saw-tooth-type potential is marked by red lines in (b). (c) Atomic geometry of the HgTe slab model. (d) The calculated density of state for (upper) the HgTe slab model and (bottom) the bulk HgTe. (e) Average and deviation values for calculated forces on each atom in HgTe thin film with the change of applied static electric field by using different methods. The deviation value is calculated for all Hg and Te atoms in the slab model.

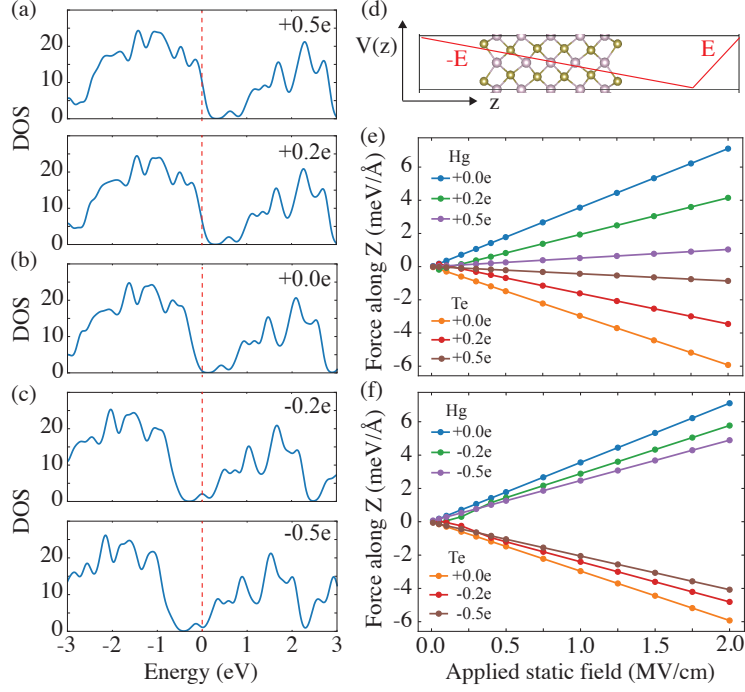


FIG. S14. The influence of screening effect on field-induced forces for the HgTe slab with charge doping. The calculated density of state for (a) the HgTe slab model with hole doping, (b) the pristine HgTe slab model, and (c) the HgTe slab model with electron doping. (d) Schematics of the saw-tooth-type potential applied to the HgTe slab model. The average values for calculated forces on each atom in the HgTe thin film with (e) hole doping and (f) electron doping under the saw-tooth-type electric potential, the force on each atom is calculated by using the length gauge field method. The dashed red lines indicate the Fermi level in (a)-(c). e is the absolute value of electron charge.

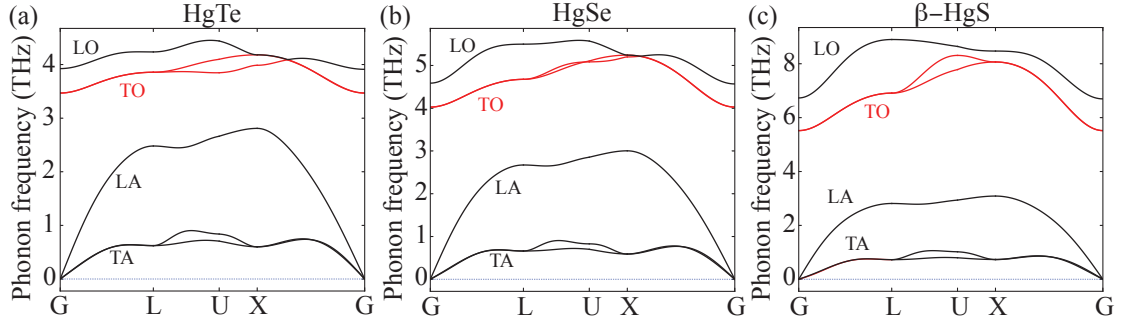


FIG. S15. Phonon dispersion of (a) HgTe, (b) HgSe, and (c) β -HgS along with symmetry points